Angewandte
International Edition Chemie

DOI: 10.1002/anie.201301468

Semiconductor Plasmonics

Engineering Multimodal Localized Surface Plasmon Resonances in Silicon Nanowires**

*Li-Wei Chou and Michael A. Filler**

There is emerging interest in nanostructured semiconductors as nontraditional plasmonic materials.[1] Importantly, the surface plasmon resonance of semiconductors, in contrast to metals, can be readily tuned through chemical doping and/or electrostatic gating.[1a,2] As carrier densities are broadly adjustable, often between 10^{19} and 10^{22} cm^{-3}, semiconductors offer resonant absorption throughout much of the infrared regime (i.e. 1–20 μm).[2c] As such, these materials are promising candidates for applications in catalysis,[3] molecular detection,[4] and energy harvesting.[5] For example, appropriately designed plasmonic semiconductors could selectively activate one or more molecular vibrational modes or resonantly capture specific bands of thermal radiation. The extensive library of techniques for processing semiconductors also presents an opportunity to fabricate complex, functional devices. Furthermore, semiconductors are often cheaper than the noble metals, which is a significant benefit for applications that require large volumes or areas.

We recently demonstrated that phosphorus-doped Si nanowires support shape-dependent mid-infrared localized surface plasmon resonances (LSPRs) with quality factors that rival the noble metals in the same spectral regime.[6] Here, we exploit the versatility of the vapor-liquid-solid technique to create Si nanowires with axially modulated dopant profiles and demonstrate user-programmable multimodal spectral responses for the first time in a nanoscale semiconductor. Our methodology provides natural axial registry of neighboring resonators and permits the tailoring of plasmonic function without altering the overall morphology.

All nanowire growth and analysis procedures are described in the Supporting Information. Briefly, Si nanowires are synthesized as schematically illustrated in Scheme 1. The nanowire diameter (*D*) is empirically controlled by the dewetting of the Au film prior to the growth of the nanowires. The aspect ratio (*A*) and phosphorus concentration of each doped segment are adjustable through the PCl_3 exposure time and the ratio (*C*) of the PCl_3 to Si_2H_6 partial pressures, respectively. The intrinsic segments near the nanowire base and tip mitigate LSPR–substrate and LSPR–catalyst interactions, respectively. We measure the spectral response of Si nanowire arrays without and with doped segments through in situ transmission infrared spectroscopy (see Figure S1 in the Supporting Information). All spectroscopic measurements occur immediately following nanowire array growth and prior to removal from the vacuum system. Buffered oxide etching (BOE) of the Si nanowires, which exhibits a phosphorus-dependent rate,[7] is used following spectral response acquisition only to confirm the presence and dimensions of each doped segment.

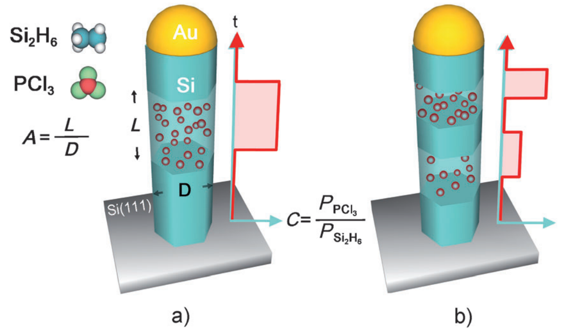

Scheme 1. A silicon nanowire containing a) single and b) multiple doped segment(s) with user-defined aspect ratios and phosphorous concentrations: *t* = growth time, *D* = nanowire diameter, *L* = length of doped segment, *A* = aspect ratio of doped segment, and *C* = ratio of the PCl_3 to Si_2H_6 partial pressures.

All nanowires, no matter the aspect ratio or phosphorous concentration of the doped segment(s), are epitaxially aligned and exhibit similar morphologies. Previous electron microscopy imaging of nanowires grown with the same precursors, temperatures, and pressures showed that these nanowires are single-crystalline.[6] The diameter (*D*) and total length of the nanowires with a single doped segment are maintained at 130 and 660 nm, respectively (Figure S2). Figure 1 a shows representative Si nanowires from arrays where the phosphorus concentration of the doped segment is nominally constant, but the aspect ratio varies between 0.4 and 3.6. While 2 minutes of buffered oxide etching is sufficient to reveal the phosphorus-doped segment, longer etching times remove the entire doped region and suggest that phosphorus atoms are well-distributed in the radial direction (Figure S3).

Figure 1 b reveals strong mid-infrared absorption features of the as-grown nanowires (i.e. prior to buffered oxide etching) that vary as a function of the doped segment geometry, and only occur for the nanowires containing phosphorus. Peak intensities increase and the absorption

---

[*] Dr. L.-W. Chou, Prof. M. A. Filler
School of Chemical & Biomolecular Engineering
Georgia Institute of Technology
311 Ferst Drive NW, Atlanta, GA 30332-0100 (USA)
E-mail: michael.filler@chbe.gatech.edu
Homepage: http://fillergroup.gatech.edu

[**] The authors gratefully acknowledge financial support from the Camille and Henry Dreyfus Postdoctoral Program in Environmental Chemistry.

Supporting information for this article is available on the WWW under http://dx.doi.org/10.1002/anie.201301468.

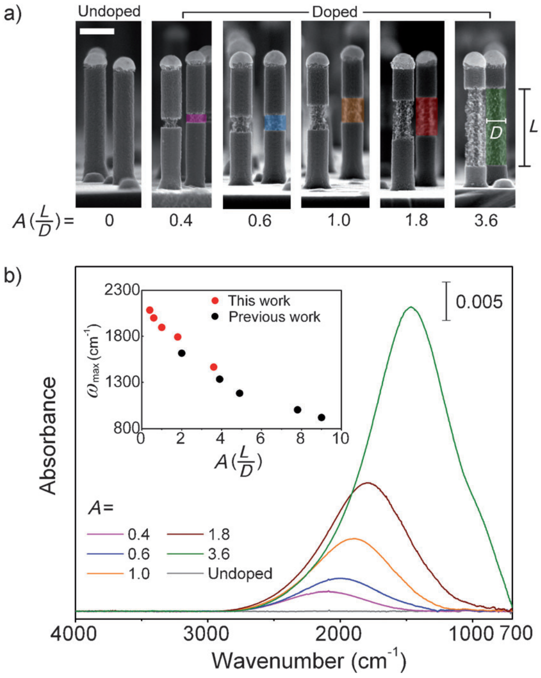

Figure 1. a) Representative cross-sectional SEM images of Si nanowires, exhibiting doped segments with systematically varied aspect ratios, acquired following buffered oxide etching for 2 minutes. Doped segments are false colored and appear rough after etching. Undoped regions straddle each doped segment and appear smooth since they etch at a significant slower rate. The scale bar is 200 nm. b) Corresponding in situ infrared absorption spectra ($\theta = 58°$) of undoped and partially doped Si nanowires recorded immediately following growth at room temperature (i.e. prior to buffered oxide etching). Inset: absorption peak maxima (ω_{max}) plotted as a function of the doped segment aspect ratio for this work (red dots) and our previously published work (black dots).[6]

maxima shift from 2080 to 1460 cm^{-1} as the doped segment aspect ratio increases. As shown in the inset of Figure 1b, these trends are consistent with our prior study of fully doped Si nanowires.[6] Angle-dependent studies show that peak intensity increases as the angle of incidence increases from 0 to 58° and indicate that the dipole is oriented parallel to the long axis of the nanowire (Figure S4). Therefore, we assign the absorption features for the present dopant-modulated nanowires to longitudinal LSPRs. Transverse (i.e. perpendicular to the nanowire axis) modes were not detected for any of the doped segments. As shown in our prior work,[6] and resulting from their inherently weak polarizability, we only anticipate sensitivity to transverse modes for doped segments with aspect ratios larger than those studied here (i.e. $A > 10$). Since the precursor partial pressure ratio and substrate temperature used here were identical to our previous study, we expect that the carrier density in the doped segments is on the order of 10^{19}–10^{20} cm^{-3}.[6]

We observe a longitudinally oriented dipole even for doped segments with an aspect ratio less than 1 (i.e. $A = 0.4$ in Figure 1). This behavior is distinct relative to low-aspect-ratio (i.e. $A < 1$) metal disks situated in low dielectric constant environments (e.g. in solution, on SiO$_2$) where the transverse mode dominates.[8] We tentatively attribute this difference to the relatively high dielectric constant of the nominally intrinsic Si segments ($\varepsilon = 11.7$) that sandwich the doped segment. Analogous to that reported for metallic particles on Si surfaces,[9] the undoped segments likely support a horizontally oriented image dipole that strongly screens the transverse LSPR. Even if the screening were partial, the short optical path length (i.e. one nanowire layer) and small polarizability volume of the $A = 0.4$ doped segment would make observation of the transverse mode challenging with our experimental setup.

Figure 2a shows representative Si nanowires where the aspect ratio of the doped segments is maintained at 1.8, but the phosphorus atom concentration varies. We adjust the phosphorus concentration by modulating the ratio of PCl$_3$ to Si$_2$H$_6$ partial pressures, defined as C in Scheme 1, between 0.007 and 0.1. Post-measurement buffered oxide etching treatments confirm that the doped segment aspect ratio is constant. However, the increase of nanowire sidewall roughening as C increases demonstrates that the phosphorus concentration positively correlates with the PCl$_3$ partial

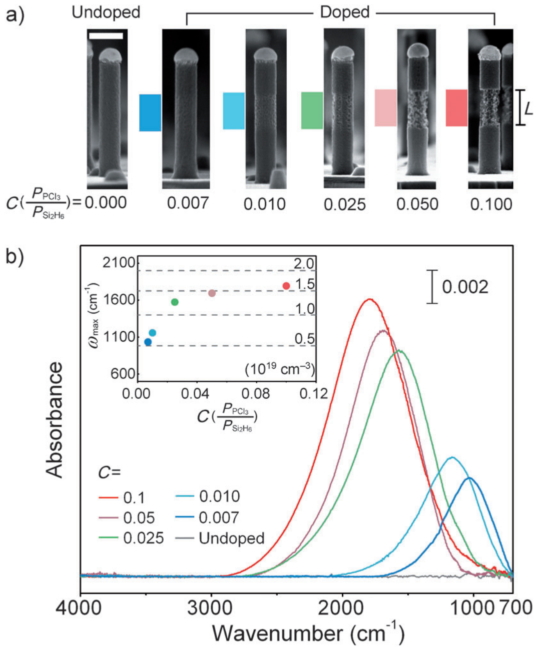

Figure 2. a) Representative cross-sectional SEM images of Si nanowires, exhibiting doped segments with systematically varied phosphorus concentrations, acquired following buffered oxide etching for 2 minutes. The stripes shown next to each doped segment correlate with the phosphorus concentration, which was controlled by varying the ratio (C) of the PCl$_3$ to Si$_2$H$_6$ partial pressures. Blue and red shades denote low and high phosphorus concentrations, respectively. Etching-induced sidewall roughening increases with phosphorus concentration. The scale bar is 200 nm. b) Corresponding in situ infrared absorption spectra ($\theta = 58°$) of undoped and partially doped Si nanowires recorded immediately following growth at room temperature (i.e. prior to buffered oxide etching). Inset: absorption peak maxima (ω_{max}) plotted as function of the ratio C. Dashed lines indicate carrier densities calculated from Mie–Gans theory.

pressure. Figure 2b displays the spectral response for arrays of each type of nanowire shown in Figure 2a. The absorption peak intensity increases and its center blueshifts from 1030 to 1790 cm^{-1} as C varies between 0.007 and 0.1. The increase in dopant concentration, and thus carrier density, results in a concomitant increase in the LSPR frequency and dipole moment. These data are consistent with prior studies of Cu_2S, Cu_2Se, Si, and Sn-doped ITO nanocrystals specifically and the assignment of LSPRs in general.[10,2c] Absorption peak maxima are plotted as a function of C in the inset of Figure 2b. Lines of constant carrier density, as determined from Mie–Gans theory assuming a Drude model for the free carriers, are also shown and indicate values on the order of 10^{19}–10^{20} cm^{-3} for the nanowires examined here. Notably, the magnitude of the blueshift asymptotes at large C values, while the etching rate continues to increase. This observation suggests that incomplete phosphorus atom ionization is occurring at large phosphorus concentrations. Although this effect currently restricts the LSPR frequency in our studies, a number of methods are known to enhance the ionization efficiency, and thus larger carrier densities ($>10^{21}$ cm^{-3}) are likely possible.[11]

We now use this knowledge to fabricate Si nanowires with multimodal spectral responses. To accomplish this, we incorporate two doped segments, each with a distinct aspect ratio and carrier density, along the length of each Si nanowire (see Scheme 1). The absorption peaks shown in Figure 3a constitute a series of monomodal LSPR building blocks and result from nanowires that contain one of five distinct doped segment types. A-type and C-type segments exhibit variable aspect ratios and carrier densities, respectively. As expected, peaks associated with A-type segments, labeled ω_A, redshift as A increases whereas those associated with C-type segments, labeled ω_C, blueshift as C increases.

Figure 3b illustrates how multimodal LSPRs arise when the A- and C-type segments shown in Figure 3a are combined into the same nanowire. We denote multimodal nanowires, for example, that combine A1- and C1-type segments as A1:C1. Importantly, vapor-liquid-solid growth ensures that each doped segment is in excellent axial registry with its neighbor. A comparison of peak positions in Figure 3a and b makes evident that each multimodal band, labeled ω_+ and ω_-, predominantly results from its monomodal LSPR building block. While multimodal LSPRs yield absorption peaks that are weaker and subtly narrower than their monomodal counterparts, a point we return to below, these prototype nanowires highlight the additive capabilities of the vapor-liquid-solid synthesis technique.

A comparison of the peak parameters for the monomodal and multimodal LSPRs reveal subtle differences that deserve further discussion (Table S1). In particular, our data show that the A- and C-type segments exhibit a non-negligible coupling interaction despite the presence of a nominally undoped spacer segment. The high frequency multimodal bands, ω_+, exhibit an average blueshift of 40 cm^{-1} and a 60% reduction of integrated intensity relative to their corresponding monomodal bands, ω_A. The low-frequency multimodal bands, ω_-, do not undergo a clear spectral shift, but display a small intensity loss when compared to their monomodal counterparts, ω_C. The random position of nanowires within the array combined with their low areal densities (of ca. 0.6 μm^2), as addressed in our previous work,[6] ensures that far-field interactions are insignificant. Since the distance separating each doped segment is on the order of the doped segment size, and much smaller than the resonance wavelength (i.e. 5–10 μm), we conclude that the coupling is largely near-field in origin.[12]

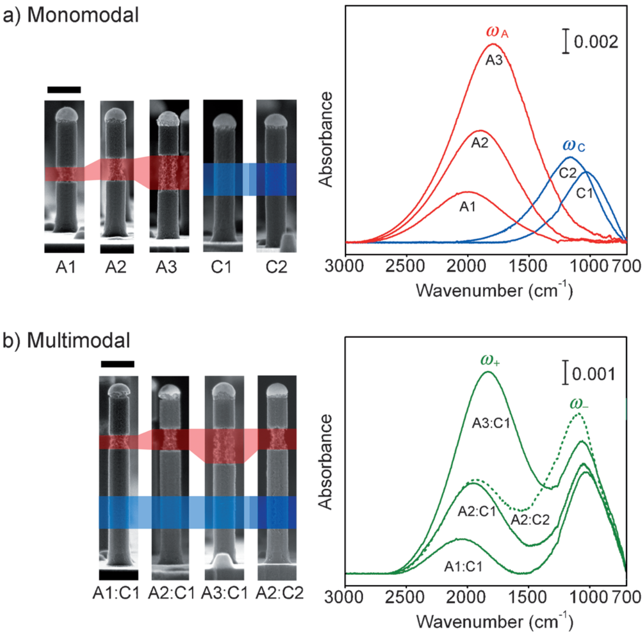

Figure 3. a) Representative cross-sectional SEM images and in situ infrared absorption spectra ($\theta = 58°$) of monomodal LSPRs originating from Si nanowires containing one doped segment. Red curves, labeled A1, A2, and A3, correspond to segments where the aspect ratio was varied ($A = 0.6$, 1.0, and 1.8) with a constant phosphorus precursor ratio ($C = 0.1$). Blue curves, labeled C1 and C2, correspond to segments where the phosphorus concentration was varied ($C = 0.007$ and 0.01) at constant aspect ratio ($A = 1.8$). ω_A and ω_C denote monomodal bands stemming from A- and C-type dopant profiles, respectively. The scale bar is 200 nm. b) Representative cross-sectional SEM images and in situ infrared absorption spectra ($\theta = 58°$) of multimodal LSPRs originating from Si nanowires that contain one A-type and one C-type segment. ω_- and ω_+ denote the low- and high-frequency multimodal bands, respectively. The scale bar is 200 nm.

Such coupling effects have been studied for metals and can be described within the context of surface plasmon hybridization theory (Figure S5)[13] More specifically, new "bonding" and "antibonding" states arise because of the near-field coupling of the A- and C-type segments. The antibonding state is higher in energy and consists of antiparallel oriented dipoles that act to reduce the overall dipole moment. Indeed, the observed blueshift and intensity loss of ω_+ relative to ω_A is consistent with this simple theoretical framework. On the other hand, the bonding state is lower in energy and exhibits dipoles oriented in a co-parallel fashion that should lead to a redshift and intensity gain of ω_- relative to ω_C. However, the observed ω_- peak frequency fluctuates within a range from -64 to $+13$ cm^{-1} with respect to ω_C (Table S1). We suspect that this behavior is a result of the incorporation of unwanted phosphorus atoms through the sidewall of the C-type segment (i.e. on the bottom and fabricated first) while the A-type segment (i.e. on the top and fabricated second) is being formed. In this situation, the C-type segment carrier density increases and leads to a blueshift that overwhelms any redshift from the coupling. When the A-type segment aspect ratio is small (e.g. A1:C1), which corresponds to a shorter PCl_3 exposure time, or the C-type segment is already more heavily doped (e.g. A2:C2), we observe the expected redshift. These findings underscore the importance of surface plasmon coupling as well as the need to control nanowire surface termination during synthesis so as to prevent the "cross-contamination" of different doped segments. Despite the prediction by hybridization theory that the bonding state peak intensity should increase, our data displays a small decrease. We continue to investigate this behavior, but note that reports of coupling in metallic systems occasionally show a similar trend.[12b,14] In addition, we observe interesting changes to the bandwidth of the multimodal LSPRs. For example, the bandwidth of the ω_+ peak for the A1:C1 combination is 200 cm^{-1} less than that of ω_A, but the ω_- mode shows little change relative to ω_C. Recent studies of stacked metallic nanodisks and nanowires with dielectric spacers revealed an analogous effect.[14a,15] While it was shown that the bandwidth decreased concomitantly with dielectric layer thickness, which identifies coupling as the root cause, the precise interaction underlying this observation remains unclear. Importantly, further investigation of near-field coupling effects in our Si nanowire arrays, specifically the observed changes in the absorption peak position, intensity, and bandwidth, will require more robust control of dopant incorporation during growth.

We also extract the quality factor (Q) and collision frequency (γ) for nanowires containing a single-doped segment (Table S2). A mean Q value of 2.6 is found for these partially doped Si nanowires, which is higher than our previously report value for fully doped Si nanowires ($Q = 1.5$). We attribute this improvement to the placement of doped segments near the center of the nanowire, which reduces the interaction of the LSPR with the Au tip and Si substrate. The Q values found here are equivalent to those reported for mid-infrared LSPRs in micrometer-long Au nanorods ($Q = 2$–3),[16,12b] but we also anticipate that a narrower distribution of nanowire diameters, achieved by patterning of the growth catalyst, will yield higher values. The measured collision frequencies decrease ($\gamma = 92$ to 48 meV) as dopant density decreases ($C = 0.1$ to 0.007) at constant aspect ratio. This trend is expected since electron-impurity scattering is reduced in lightly doped materials.[17]

In conclusion, we demonstrate that the bottom-up vapor-liquid-solid technique is an excellent synthetic platform with which to engineer multimodal plasmonic responses in semiconductors. Our approach provides a straightforward method to incorporate multiple, dimensionally controlled, and axially registered plasmonic domains along the length of individual nanowires. The Q values reported here, which are equivalent to those for the noble metals in this spectral regime, highlight the potential of this well-established semiconductor for studying basic surface plasmon physics or advancing applications including catalysis, molecular sensing, and energy harvesting.

Received: February 19, 2013
Revised: May 20, 2013

Keywords: doping · nanowires · semiconductor plasmonics · silicon · surface plasmon resonances

---

[1] a) D. Li, C. Z. Ning, *Opt. Express* **2011**, *19*, 14594–14603; b) G. V. Naik, A. Boltasseva, *Metamaterials* **2011**, *5*, 1–7; c) A. Boltasseva, H. A. Atwater, *Science* **2011**, *331*, 290–291; d) Y. Zhao, C. Burda, *Energy Environ. Sci.* **2012**, *5*, 5564–5576.

[2] a) R. J. Walters, R. V. A. van Loon, I. Brunets, J. Schmitz, A. Polman, *Nat. Mater.* **2010**, *9*, 21–25; b) G. Garcia, R. Buonsanti, E. L. Runnerstrom, R. J. Mendelsberg, A. Llordes, A. Anders, T. J. Richardson, D. J. Milliron, *Nano Lett.* **2011**, *11*, 4415–4420; c) J. M. Luther, P. K. Jain, T. Ewers, A. P. Alivisatos, *Nat. Mater.* **2011**, *10*, 361–366.

[3] a) Y.-F. Huang, H.-P. Zhu, G.-K. Liu, D.-Y. Wu, B. Ren, Z.-Q. Tian, *J. Am. Chem. Soc.* **2010**, *132*, 9244–9246; b) S. Linic, P. Christopher, D. B. Ingram, *Nat. Mater.* **2011**, *10*, 911–921; c) M. Sun, Z. Zhang, H. Zheng, H. Xu, *Sci. Rep.* **2012**, *2(647)*, 1–4.

[4] a) R. F. Aroca, D. J. Ross, C. Domingo, *Appl. Spectrosc.* **2004**, *58*, 324A–338A; b) R. Adato, A. A. Yanik, J. J. Amsden, D. L. Kaplan, F. G. Omenetto, M. K. Hong, S. Erramilli, H. Altug, *Proc. Natl. Acad. Sci. USA* **2009**, *106*, 19227–19232.

[5] a) H. A. Atwater, A. Polman, *Nat. Mater.* **2010**, *9*, 205–213; b) W. Chihhui, N. Burton III, J. Jeremy, M. Andrew, Z. Byron, S. Steve, S. Gennady, *J. Opt.* **2012**, *14*, 024005.

[6] L.-W. Chou, N. Shin, S. V. Sivaram, M. A. Filler, *J. Am. Chem. Soc.* **2012**, *134*, 16155–16158.

[7] a) K. R. Williams, R. S. Muller, *J. Microelectromech. Syst.* **1996**, *5*, 256–269; b) N. Valckx, D. Cuypers, R. Vos, H. Philipsen, J. Rip, G. Doumen, P. Mertens, M. Heyns, S. D. Gendt, *Solid State Phenom.* **2012**, *187*, 187.

[8] a) B. Nikoobakht, M. A. El-Sayed, *Chem. Mater.* **2003**, *15*, 1957–1962; b) W. Rechberger, A. Hohenau, A. Leitner, J. R. Krenn, B. Lamprecht, F. R. Aussenegg, *Opt. Commun.* **2003**, *220*, 137–141; c) K. Ueno, V. Mizeikis, S. Juodkazis, K. Sasaki, H. Misawa, *Opt. Lett.* **2005**, *30*, 2158–2160.

[9] a) S.-Y. Chen, J. J. Mock, R. T. Hill, A. Chilkoti, D. R. Smith, A. A. Lazarides, *ACS Nano* **2010**, *4*, 6535–6546; b) H. Chen, T. Ming, S. Zhang, Z. Jin, B. Yang, J. Wang, *ACS Nano* **2011**, *5*, 4865–4877.

[10] a) M. Kanehara, H. Koike, T. Yoshinaga, T. Teranishi, *J. Am. Chem. Soc.* **2009**, *131*, 17736–17737; b) Y. Zhao, H. Pan, Y. Lou, X. Qiu, J. Zhu, C. Burda, *J. Am. Chem. Soc.* **2009**, *131*, 4253–4261; c) D. Dorfs, T. Haertling, K. Miszta, N. C. Bigall, M. R. Kim, A. Genovese, A. Falqui, M. Povia, L. Manna, *J. Am. Chem. Soc.* **2011**, *133*, 11175–11180; d) D. J. Rowe, J. S. Jeong, K. A. Mkhoyan, U. R. Kortshagen, *Nano Lett.* **2013**, *13*, 1317–1322.

[11] a) M. Finetti, P. Negrini, S. Solmi, D. Nobili, *J. Electrochem. Soc.* **1981**, *128*, 1313–1317; b) A. Yamada, Y. Jia, M. Konagai, K. Takahashi, *Jpn. J. Appl. Phys.* **1989**, *28*, L2284.

[12] a) R. Taubert, R. Ameling, T. Weiss, A. Christ, H. Giessen, *Nano Lett.* **2011**, *11*, 4421–4424; b) D. Weber, P. Albella, P. Alonso-González, F. Neubrech, H. Gui, T. Nagao, R. Hillenbrand, J. Aizpurua, A. Pucci, *Opt. Express* **2011**, *19*, 15047–15061.

[13] a) B. Willingham, D. W. Brandl, P. Nordlander, *Appl. Phys. B* **2008**, *93*, 209–216; b) P. K. Jain, M. A. El-Sayed, *Chem. Phys. Lett.* **2010**, *487*, 153–164; c) L. S. Slaughter, Y. Wu, B. A. Willingham, P. Nordlander, S. Link, *ACS Nano* **2010**, *4*, 4657–4666.

[14] a) A. Dmitriev, T. Pakizeh, M. Käll, D. S. Sutherland, *Small* **2007**, *3*, 294–299; b) C. Wadell, T. J. Antosiewicz, C. Langhammer, *Nano Lett.* **2012**, *12*, 4784–4790.

[15] R. Taubert, Ph.D. thesis, Universität Stuttgart **2012**.

[16] F. Neubrech, D. Weber, R. Lovrincic, A. Pucci, M. Lopes, T. Toury, M. L. de La Chapelle, *Appl. Phys. Lett.* **2008**, *93*, 163105-1–163105-3.

[17] a) E. Conwell, V. F. Weisskopf, *Phys. Rev.* **1950**, *77*, 388–390; b) K. Seeger, *Semiconductor Physics: An Introduction*, Springer, Heidelberg, **2004**.